

Bright single-photon source in a silicon chip by nanoscale positioning of a color center in a microcavity

Baptiste Lefaucher,^{†,§} Yoann Baron,^{‡,§} Jean-Baptiste Jager,[†] Vincent Calvo,[†]
Christian Elsässer,[†] Giuliano Coppola,[†] Frédéric Mazen,[‡] Sébastien Kerdilès,[‡] Félix
Cache,[¶] Anaïs Dréau,[¶] and Jean-Michel Gérard^{*,†}

[†]*Univ. Grenoble Alpes, CEA, Grenoble INP, IRIG, PHELIQS, 38000 Grenoble, France*

[‡]*Univ. Grenoble Alpes, CEA-LETI, Grenoble 38000, France*

[¶]*Laboratoire Charles Coulomb, Université de Montpellier and CNRS, Montpellier, France*

[§]*Contributed equally to this work*

E-mail: jean-michel.gerard@cea.fr

Abstract

We present an all-silicon source of near-infrared linearly-polarized single photons, fabricated by nanoscale positioning of a color center in a silicon-on-insulator microcavity. The color center consists of a single W center, created at a well-defined position by Si⁺ ion implantation through a 150 nm-diameter nanohole in a mask. A circular Bragg grating cavity resonant with the W's zero-phonon line at 1217 nm is fabricated at the same location as the nanohole. Under above-gap continuous-wave excitation, a very clean photon antibunching behavior ($g^2 \leq 0.06$) is observed over the entire power range, which highlights the absence of parasitic emitters. Purcell-enhancement of W's zero-phonon emission provides both a record-high photoluminescence count rate among

Si color centers (ca 1.2×10^6 counts/s) and apparent Debye-Waller factor around 99%. We also demonstrate the triggered emission of single photons with 93% purity under weak pulsed laser excitation. At high pulsed laser power, we reveal a detrimental effect of repumping processes, that could be mitigated using selective pumping schemes in the future. These results represent a major step towards on-demand sources of indistinguishable near-infrared single photons within silicon photonics chips.

Introduction

The generation, processing, and detection of single photons have enabled pioneering investigations in quantum physics, paving the way to groundbreaking technologies. Silicon quantum photonics, namely the processing of photonic quantum states in a silicon chip, is at the forefront of this revolution.^{1,2} However, the potential of silicon photonics for large-scale quantum applications is limited by the difficulty to deterministically generate arbitrary large entangled photon states on-chip. A key requirement to overcome this limitation is to embed sources of indistinguishable single photons operating on demand. While integrated sources of entangled photon pairs based on spontaneous four-wave mixing have enabled major demonstrations,² these sources suffer from an inherent interplay between efficiency and multi-photon pairs emission. Alternative approaches rely on fiber-coupling of an external source,^{3,4} and hybrid integration of quantum emitters,⁵⁻⁷ albeit with limited efficiency due to coupling losses.

In this context, near-infrared color centers in silicon have emerged as a promising path towards deterministic single-photon sources (SPS) circumventing coupling losses. Due to their emission wavelength in the telecom bands, these point defects also appear as potential sources for chip-based quantum communications. Since the observation of photon antibunching for single color centers in 2020,^{8,9} tremendous efforts have been devoted to optimizing their elaboration processes,¹⁰⁻¹⁴ and exploring their photophysical properties.¹⁵⁻¹⁹ In order to build a SPS, it is necessary to embed the emitter in a photonic cavity to achieve on-

demand emission of single photons in a well-defined optical mode using the Purcell effect.²⁰ Several single-mode sources in silicon have been demonstrated, based on a T center,^{21,22} G center,²³ G^{*} center,²⁴ and erbium dopant.²⁵ However, in spite of remarkable improvement of emission properties owing to a high Purcell factor, these sources suffer from significant limitations. The T center and erbium dopant are inherently slow emitters,^{21,22} the G center has a poor quantum efficiency,^{23,26,27} and the fabrication process of the G^{*} center is not selective,¹⁵ resulting in poor purity due to the presence of parasitic defects.²⁴ Moreover, in these first experiments the position of the emitter in the cavity is not controlled, hindering both the optimal exploitation of the Purcell effect and the reproducible fabrication of the SPS.

In recent work, Purcell enhancement has been demonstrated for an ensemble of W centers in circular Bragg grating (CBG) cavities in a silicon-on-insulator (SOI) film.^{28,29} On the one hand, these results have positioned the W center as a promising candidate to build a SPS, owing to its high quantum efficiency ($\approx 2/3$) and relatively fast zero-phonon emission ($\tau_{ZPL} \approx 134$ ns) in bulk silicon.²⁸ On the other hand, it confirms that CBG cavities, which have been widely used in other material systems,^{30–35} are also attractive for building SPS on SOI chips.

In this letter, we present a SPS fabricated by nanoscale positioning of a single W center in a SOI CBG cavity. An array of W centers is created by Si⁺ ion implantation through a mask patterned with nanoholes,¹¹ then an array of CBG cavities centered at the same location as the nanoholes and resonant with the W zero-phonon line (ZPL) is fabricated. The optical properties of a cavity-coupled W center are studied by photoluminescence (PL) spectroscopy and photon correlation measurements under above-gap continuous-wave (CW) and pulsed excitation. The purity of the source is analyzed as a function of the laser excitation power.

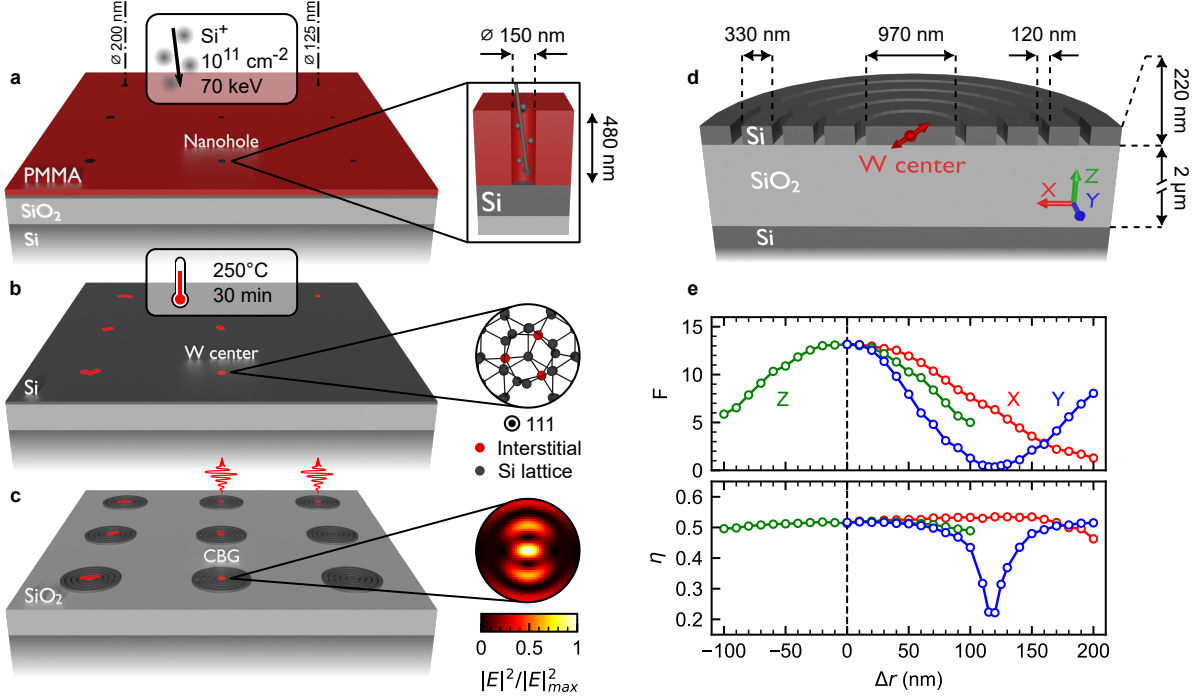


Figure 1: **Integration of W centers in circular Bragg grating cavities, and expected cavity effects.** **a**, Implantation of Si^+ ions in SOI through a PMMA layer patterned with nanoholes. **b**, Activation of the W centers by thermal annealing. The microscopic structure of the W center is shown in the inset. **c**, Fabrication of CBG cavities centered on the nominal coordinates of the nanoholes. The intensity of the electromagnetic field in the central disk is shown in the inset. **d**, Schematic sectional view of a CBG cavity containing a single W center, with the relevant dimensions. The red double-arrow indicates the orientation of the transition dipole. **e**, Normalized spontaneous emission rate F and collection efficiency η for a numerical aperture of 0.65, as a function of the algebraic distance Δr between the dipole and the center of the cavity in the coordinate system shown in **d**.

Sample design and fabrication

A 480 nm-thick mask of polymethyl methacrylate (PMMA) is deposited onto a commercial piece of SOI wafer. Arrays of nanoholes defined by electron beam lithography are etched into the mask. The sample is then broad-beam implanted with Si^+ ions (Figure 1(a)). A similar approach has already proven efficient for the fabrication of NV centers at preset positions in diamond,^{36,37} and, more recently, G and W centers in silicon.¹¹ The PMMA mask is then removed by stripping with acetone and the sample is annealed at 200 °C for 30 minutes in N_2 atmosphere (Figure 1(b)). This second step leads to the activation of

the W center,^{38,39} whose microscopic structure (consisting of three interstitial Si atoms) is shown in the inset. A characterization of the emitters in unpatterned SOI is presented in Section 3 of the Supporting Information. CBG cavities centered at the same location as the nanoholes are fabricated by electron beam lithography and reactive ion etching (Figure 1(c)). This method is well-trying for the high-yield fabrication of SPS based on III-V semiconductor quantum dots (QD).^{40,41} A map of the electromagnetic field in the central disk of the cavity is shown in the inset. After fabrication, the sample is first inspected by scanning electron microscopy, to confirm successful fabrication according to design parameters (see Figure S11 in the Supporting Information).

A sectional view of a CBG cavity containing a single W center is schematically represented in Figure 1(d), with the relevant dimensions. The red double-arrow represents the orientation of the transition dipole along the $\langle 111 \rangle$ direction.¹⁶ It is well-known for CBG cavities that the Purcell enhancement factor F , defined as the ratio between the emission rate in the cavity and bulk semiconductor, is heavily dependent on the position of the emitter.⁴⁰ This sensitivity was investigated for our emitter-cavity system using numerical finite-difference time-domain simulations (FDTD, see Section 4 in the Supporting Information). Figure 1(e) shows the Purcell enhancement factor for the ZPL as a function of the distance Δr between the center of the cavity and the position of the dipole, in the coordinate system defined in Figure 1(d). A maximum enhancement factor of 13 is obtained at the center of the cavity. F decreases rapidly against Δr and reaches 0.3 for $|\Delta Y| = 120$ nm, emphasizing the requirement for high positioning accuracy. Considering the simulated lateral spread of the ions implanted through a nanohole of 150 nm diameter, we estimate that the W centers have near-unity probability to be located less than 120 nm away from the center of the cavity, i.e. in the vicinity of the main antinode of the electromagnetic field (see Section 2 in the Supporting Information).

The collection efficiency for a cavity-coupled W center was also investigated using FDTD, considering the configuration of our measurement setup. The fraction η of dipole emission radiated through a numerical aperture of 0.65 at normal incidence is plotted against Δr in

Figure 1(e). A collection efficiency of 51% is obtained at the center of the cavity. Note that this value could be increased to nearly 100% with the addition of a high-reflectivity mirror below the cavity.⁴² The curves also reveal the robustness of the collection efficiency against spatial detuning (with $\eta > 44\%$ for $\Delta r \leq 100$ nm for each three coordinates), except for the "pit" around $|\Delta Y| = 120$ nm where the emitter is at an antinode of the electromagnetic field. This feature makes CBG cavities an attractive microstructure to easily increase the photon detection rate from quantum emitters in SOI. Similarly, the collection efficiency is also found robust against spectral detuning (see Figure S7 in the Supporting Information).

Experimental results

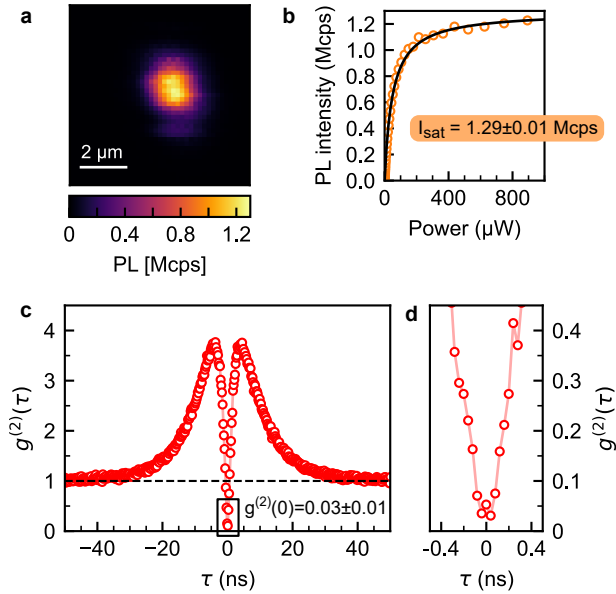


Figure 2: **Observation of a single W center in a CBG cavity.** **a**, PL map of a single W center in a CBG cavity at saturation under CW excitation. **b**, PL saturation curve for the W in the CBG cavity under above-gap CW excitation. The PL intensity is integrated over the 1200 - 1300 nm spectral range. The black line is a fit to the saturation function for a two-level system, $I = I_{sat}/(1 + P_{sat}/P)$, with $I_{sat} = 1.29 \pm 0.01$ Mcps and $P_{sat} = 49 \pm 1$ μ W. **c**, Second-order photon correlation histogram of the PL emission for $P = 135 \mu$ W. **d**, A zoom at short time delays reveals a $g^{(2)}(0)$ value of around 0.03.

After fabrication, the sample is characterized by mapping the PL intensity in the emission

range of W centers. On PL maps, CBG cavities that contain W centers appear as bright spots on a black background (Figure 2(a)). As the number of W centers formed through localized ion implantation is a random variable, we have thus to identify the CBG cavities that contain a single W center. Since the PL emission of single W centers, collected under normal incidence, is linearly polarized along either $[110]$ or $[1\bar{1}0]$ crystal axes of Si, we identify very easily the CBG cavities that are the most likely to contain a single W emitter, by comparing two polarized-resolved PL maps, obtained for those crossed polarizations (see Section 5 in the Supporting Information). Photon-autocorrelation experiments in the Hanbury Brown and Twiss configuration are then performed to confirm the presence of one and only one W center in the cavity.

We display in Figure 2 a typical set of results obtained for a CBG cavity containing a single W center under above-gap CW excitation (see Section 1 in the Supporting Information for details about the measurement configuration). A measurement of the polarization diagram of the PL evidences linear polarization along the $[110]$ axis of the silicon crystal with 97.2 ± 0.7 % visibility (see Figure S9 in the Supporting Information). We observe of a clean antibunching dip in the photon-autocorrelation histogram shown in Figure 2(c, d). It is worth emphasizing that this low value of $g^{(2)}(0)$ is obtained without any correction for detectors dark counts or background emission. A bunching behaviour ($g^{(2)}(\tau) > 1$) is observed at non-zero delay. This phenomenon, already reported for single W centers,^{11,16} is attributed to a metastable state coupled to the excited state of the emitter.

In order to highlight cavity effects on the single W center emission, we also show in Figure 2(b) a study of the PL intensity as a function of the CW pump power. We observe a well defined saturation behaviour and a count rate at saturation around 1.29 ± 0.01 Mcps. This value is remarkably high compared to previously published results for other color centers in SOI, as shown in Table 1. Importantly, we observe a very low $g^{(2)}(0)$ over the full range of pump powers up to the saturation plateau ($g^{(2)}(0)$ is equal to 0.03 at $3 P_{sat}$ and to 0.06 at $9 P_{sat}$), unlike most previous reports. This important observation confirms that

Table 1: Comparison between this work and previous reports of cavity-enhanced single-photon emitters in silicon under CW pumping. Em.: emitter. Cav.: cavity. Pos.: nanoscale positioning of the emitter. PhC: photonic crystal cavity. We give for T and W results obtained at 2 different powers that either provide maximum I_{PL} or minimum $g^{(2)}(0)$ value.

Em.	Cav.	I_{PL} (kcps)	τ (ns)	$g^{(2)}(0)$	Pos.	Reference
G*	2D PhC	20	6.7	0.30	No	Redjem et al. ²⁴
G	2D PhC	20	6	0.03	No	Saggio et al. see SI in ref.[23]
T	1D PhC	20	169	0.07	No	Islam et al. ²¹
		236		0.35		
W	CBG	940	7	0.03	Yes	This work
		1200		0.06		

our fabrication process does not produce parasitic emitters, besides the desired isolated W center. The beneficial effect of the CBG cavity is most obviously evidenced by comparing the latter PL count rate at saturation to the one of isolated W centers in unpatterned SOI which is typically around 3.2 ± 0.8 kcps after correction for background counts rate (see Section 3 in the Supporting Information). This represents an enhancement factor of around 400 for the PL count rate thanks to cavity effects. As shown below, this increase results from the combination of Purcell-enhancement of zero-photon emission into the CBG cavity mode and the small divergence of the radiation pattern of this mode in the far-field, providing efficient collection of zero-phonon emission.

To understand quantitatively cavity effects, we investigated the properties of the cavity mode and the spectral resonance of the emitter-cavity system. The modal properties have been probed by performing reflection spectroscopy under white light illumination. As shown in Figure 3(b), the reflectivity curve features a dip around 1218 nm, fitting to a Lorentzian profile with a full width at half maximum (FWHM) $\Delta\lambda_m = 7.7 \pm 0.2$ nm, corresponding to a quality factor $Q = 158 \pm 5$. This value is in good agreement with the quality factor estimate of 167 obtained from FDTD simulations. The CBG cavity mode is therefore nearly perfectly matched to the ZPL emission of zero-phonon emission line of W centers in unstrained silicon,¹⁶ as confirmed from a comparison of reflectivity and PL emission spectra in Figure 3(a). Noticeably, this PL spectrum over the 1140-1450 nm spectral range reveals

that zero-phonon emission accounts for $\xi = 98.6\%$ of the PL intensity, value to be compared with 39% for isolated W in unpatterned SOI, which unveils a selective enhancement of ZPL emission thanks to the Purcell effect.

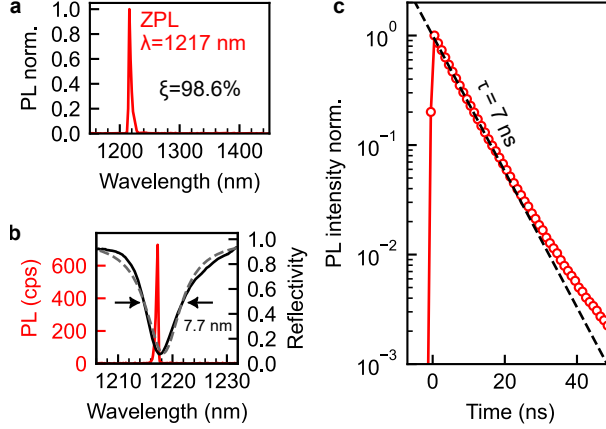


Figure 3: **Optical properties of a CBG-coupled W center.** **a**, PL spectrum in the 1150 - 1450 nm spectral range. **b**, High-resolution PL spectrum and white-light reflectometry measurement of the cavity. The dashed grey line is a fit to a Lorentzian profile. **c**, PL decay of the emitter under triggered excitation with a repetition rate of 5 MHz and $17.5 \mu\text{W}$ average power.

We study now the recombination dynamics of the W center to estimate the magnitude of the Purcell effect. The PL decay of the emitter under pulsed excitation at $17.5 \mu\text{W}$ with a 5 MHz repetition rate is displayed in Figure 3(c). The intensity decays nearly mono-exponentially with a characteristic time $\tau = 7 \pm 1 \text{ ns}$. This value should be compared with the characteristic time of around 34 ns obtained for ensembles of W centers in unpatterned SOI.^{28,29,39} The acceleration of the decay compared to this reference value has two possible origins: Purcell enhancement of zero-phonon emission, and/or activation of extra non-radiative recombination channels due to the interaction between the emitter and its environment. This second possibility cannot be neglected *a priori* as a significant lifetime dispersion has been reported for single W centers in 60 nm-thick SOI,¹⁶ although this dispersion can likely be attributed to surface effects in such a thin SOI layer. A detailed analysis of the photon budget, from emission by W centers to detection by our single photon detectors, provides a lower-bound estimate around $1/18 \text{ ns}^{-1}$ for the zero-phonon emission rate (see

Section 6 in the Supporting Information). By comparison with a previous estimate of $1/134 \text{ ns}^{-1}$ in bulk Si,²⁸ we conclude that the zero-phonon emission rate is increased by a factor $F > 7.2$. Therefore, the acceleration of the PL decay results predominantly (and possibly entirely) from the Purcell effect. Additionally, according to Figure 1(e), we can also conclude that the emitter is positioned less than 100 nm away from the cavity center.

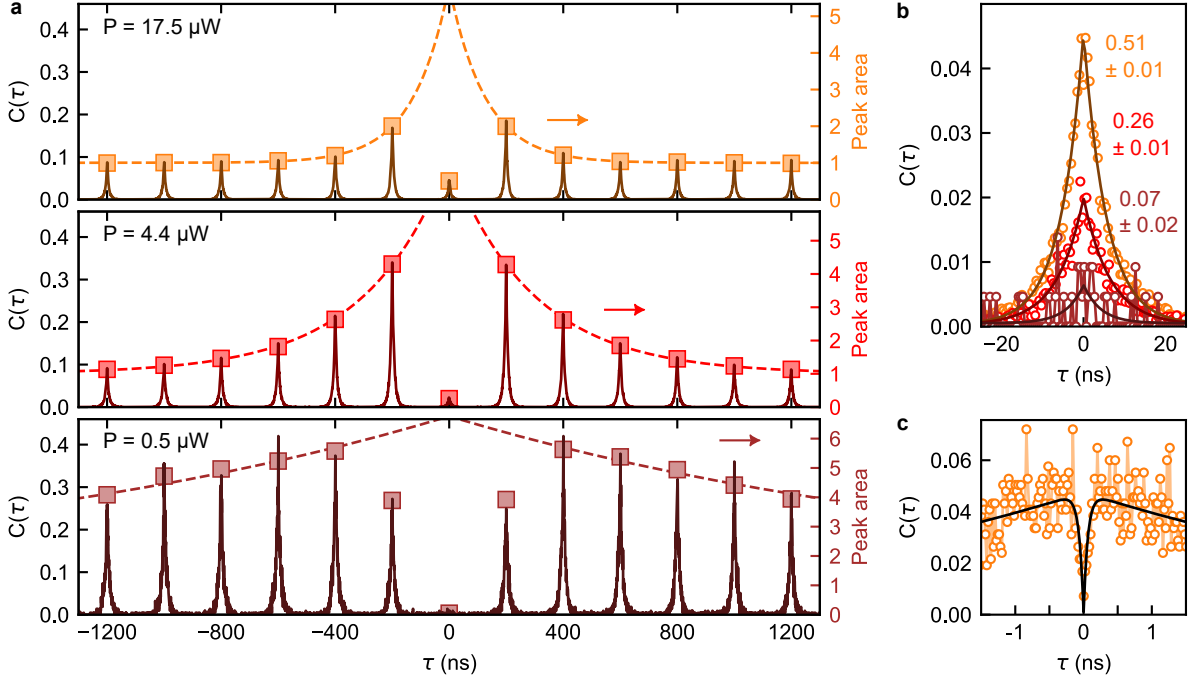


Figure 4: **Triggered single photons from a CBG-coupled W center.** **a**, Second-order correlation histogram $C(\tau)$ for $P = 0.5, 4.4$ and $17.5 \mu\text{W}$. The normalized area of each peak is given by the coordinate of the filled squares on the right axis. The dashed lines represent a fit of the peaks area to Equation 1. **b**, Zoom on the central peak. The numbers indicate the area of the peak for each power value. **c**, Zoom on the central peak for $P = 17.5 \mu\text{W}$ with 20 ps time-bins.

The bright emission of antibunched photons under CW excitation unveils the strong potential of W centers for building a deterministic SPS in SOI. Along this line, we have explored the triggered emission of single photons under pulsed excitation. Figure 4(a) shows uncorrected autocorrelation histograms obtained for different pump powers for a 5MHz repetition rate. In this figure, histograms are normalized such that the area of all peaks would be equal to 1 for a coherent source. The normalized area A_m as a function of time delay mT , where

T is the laser repetition period, of each peak is given by the coordinate of the squares on the right axis. In the low power regime, the peak at zero-delay has an area $A_m = 0.07 \pm 0.02$, demonstrating the triggered emission of single-photon pulses with 93% purity. As for the measurement under CW excitation, a bunching behaviour is observed ($A_m > 1$), indicating photoblinking of the source. Note that this effect is a rather common issue for solid-state quantum emitters and is expected for W, as this color center possesses a metastable excited state.¹⁶ The area A_m of the peaks follows an exponential law given by:

$$A_{m \neq 0} = 1 + \frac{\tau_{off}}{\tau_{on}} e^{-(1/\tau_{off} + 1/\tau_{on})|mT|} \quad (1)$$

where τ_{on} and τ_{off} are the average times of stay of the emitter in the "bright" and "dark" states, respectively.⁴³ For $P = 0.5, 4.4, \text{ and } 17.5 \mu\text{W}$, $\tau_{on} = 2290, 341, \text{ and } 153 \text{ ns}$, and $\tau_{off} = 13200, 2200, \text{ and } 741 \text{ ns}$, pointing towards an acceleration of the blinking with increasing power. Interestingly, the peaks for $|m| = 1$ have a smaller area than expected from the model in the low-power regime. This effect, which has been reported for single InAs QD under above-gap excitation,⁴⁴ may be related to a two-step transition from the ground state to the excited state, which is indeed predicted by ab-initio calculation.¹⁶

The area A_0 of the central peak increases with power, as shown in Figure 4(b). For $P = 17.5 \mu\text{W}$, the area of the peak reaches 0.51, meaning that about two photons are emitted on average per excitation pulse. A zoom on the peak with 20 ps time bins (Figure 4(c)) reveals an antibunching dip with a characteristic time of $\approx 60 \text{ ps}$ (that disappears in Figure 4(b) due to rebinning). This antibunching behaviour indicates that the two photons are emitted successively. An explanation is that, under strong above-gap pumping condition, a second exciton can be captured after the emission of a first photon, as reported for other quantum emitters.⁴⁵ This phenomenon is not surprising here, due to the optical injection of a large population of carriers by the pump pulse in the central disk of the cavity. As for QD-SPS, we expect to overcome this limitation through the implementation of resonant or quasi-resonant

pumping schemes.

Present limitations and development prospects

Under pulsed excitation at 5MHz frequency, the PL count rate reaches 52 kcps at saturation. This value corresponds, after taking into account transmission losses, to a source efficiency ϵ (as measured at the first lens of our collection optics) comprised between 0.03 and 0.06 photon per pulse (see Section 6 of the SI). The main factors limiting ϵ at this stage are easily identified: (1) W is in its bright state one sixth of the time, which reduces its average efficiency by the same amount; (2) our CBG cavity funnels only one-half of the emission towards our collection optics; (3) parasitic recombination channels (non-radiative ones and to a lesser extent phonon-assisted recombination) reduce the quantum efficiency η_{ZPL} of the zero-phonon emission to a value comprised between 0.36 and 0.68.

While point (1) and the issue of blinking has already been discussed, we see that points (2) and (3) can be radically improved by replacing our low-Fp CBG cavity by a high-Fp waveguide-coupled photonic crystal cavity, such as a nanobeam cavity.^{21,22,46} Proper engineering of light extraction towards the waveguide mode and a large but realistic Purcell factor around 150 would bring the zero-phonon emission rate above 10^9 s^{-1} . This would ensure that the quantum efficiency of the ZPL, the spontaneous emission factor β and the efficiency of the waveguide-coupled SPS are all near unity. Single photon coherence and indistinguishability are also required properties for applications to quantum simulations and computing. Until now, Hong-Ou-Mandel interference have only been demonstrated over relatively narrow time-windows, shorter than the emitter lifetime.⁴⁷ Combining such a large Purcell acceleration of zero-phonon emission, with strategies aiming at reducing dephasing processes (such as quasi-resonant pumping or the application of a static electric field), will likely permit to generate highly-indistinguishable photons on demand.

From a technological point of view, our strategy for positioning single W centers is fully compatible with the geometry of photonic crystal cavities. In order to fully benefit from

their large Purcell-enhancement factor, one has to implement means enabling a fine control of the spectral detuning between W's ZPL and the high-Q cavity mode. In this context, electrical and strain tuning of the ZPL have been recently demonstrated for G centers.^{48,49}

Conclusion

In conclusion, we have demonstrated a source of near-infrared linearly-polarized single photons obtained by nanoscale positioning of a W center in a SOI CBG cavity. Si⁺ implantation through a mask patterned with nanoholes allows for selective creation of single W centers, positioned in the vicinity of the main antinode of the resonant mode. The cavity-coupled emitter has a PL intensity at saturation of around 1.2 Mcps together with a $g^{(2)}(0)$ value of around 0.06 under above-gap CW excitation, with a ZPL fraction of 98.6%. Under weak pumping condition, the triggered emission of single-photon pulses is demonstrated with 93% purity. These results highlight the great potential of W centers for silicon quantum photonics. They pave the way towards the scalable integration of bright sources of indistinguishable single photons on integrated photonic chips, based on single W centers deterministically positioned in high-Fp waveguide-coupled photonic crystal nanocavities.

Methods

Sample preparation. The silicon layer and buried oxide layer of our SOI have a thickness of 220 nm and 2 μm , respectively. The PMMA layer is chosen thick enough (480 nm) to stop the Si⁺ ions with nearly 100% probability during the implantation (see Figure S3 in the Supporting Information). The nanoholes etched into the mask have diameters ranging from 125 nm to 2 μm (see Table S1 in the Supporting Information), and 10 μm pitch between the holes. The implantation of Si⁺ ions is performed at an energy of 70 keV, with a dose of 10^{11} cm^{-2} and 7° tilt to avoid channeling.

Experimental setup. The full optical measurement setup is schematically represented in SI Section 1. The sample is cooled at 10 K in a helium-flow cryostat (Oxford Instruments Microstat HiRes). Continuous-wave and pulsed optical excitation are provided by a semiconductor laser (PicoQuant LDH-IB-485-B) operating around 485 nm. In pulsed operation mode, the pulses have a full-width at half-maximum (FWHM) of 100 ps and tunable repetition rate. The laser beam is coupled into a single-mode fiber for spatial filtering, and collimated using a microscope objective mounted onto a translation stage in order to finely control the divergence of the beam. The laser is focused onto the sample to a $1/e^2$ -spot diameter of ≈ 700 nm using a microscope objective with a numerical aperture of 0.65 (Olympus LCPLN50XIR). The objective is mounted onto a tri-axial positioner allowing for 50 nm translation steps for photoluminescence (PL) mapping. A visualization line is accessible using a removable beamsplitter, in order to obtain an image of the sample on a CCD camera for alignment procedures.

The PL is collected using the microscope objective and separated from the laser using a dichroic mirror with a cutoff wavelength of 650 nm. The 1200 - 1300 nm spectral range is selected through a combination of longpass and shortpass filters, and the PL is focused into a single-mode fiber using a reflective collimator (Thorlabs RC04APC-P01). The PL is detected using superconducting nanowire single-photon detectors (SNSPD, ID Quantique ID281), with a detection efficiency of 81% for Detector 1 at 1310 nm (resp. 86% for Detector 2), dark count rate of 9 cps (resp. 8 cps), and timing jitter of 29 ps (resp. 30 ps). The polarization of the photons impinging on the SNSPD is controlled using a half-waveplate and a fiber polarization controller for optimized detection efficiency for both detectors. The photon detection events are counted by a time-correlated single-photon counting card (PicoQuant MultiHarp 150). For second-order correlation measurements, the card is operated in a time-tagged time-resolved mode.

For spectral measurements, the PL is dispersed by a grating with 900 lines/mm in a spectrometer (Horiba JY iHR320) and detected by a linear InGaAs array (Horiba 81043

Spectrum One). The system has a spectral resolution of 0.4 nm.

For polarization-resolved measurements, a motorized half-waveplate is placed in front of a polarizing beamsplitter cube (PBS). The PBS has a transmission of 98.2% for P-polarized light and 0.135% for S-polarized light at 1218 nm. The intensity is recorded as a function of the angle θ between the axis of the half-waveplate and the transmission axis of the PBS. The intensity is plotted as a function of 2θ to reconstruct the polarization diagram of the PL.

For reflectometry measurements, white-light from a tungsten source is injected into a single-mode fiber and collimated using a reflective collimator. A 50:50 removable beamsplitter cube is used to inject the white beam into the excitation line, and the reflected light is collected using the same collection line as for the PL.

Acknowledgement

We thank Guillaume Cassabois and Vincent Jacques for fruitful discussions, as well as Krithika V. R. and Alicia Morandini for experimental support. This work is supported by the Plan France 2030 through the project OQuLuS (No. ANR-22-PETQ-0013), the French National Research Agency (ANR) through the projects OCTOPUS (No. ANR-18-CE47-0013-01) and WOUAH (No. ANR-24-CE47-4667), CEA through the PTC-MP “W-TeQ” internal project, and the European Research Council (ERC) under the European Union’s Horizon 2020 research and innovation programme (project SILEQS, Grant No. 101042075). B.L. is supported by the “Program QuantForm-UGA No. ANR-21-CMAQ-003 France 2030” and “Laboratoire d’Excellence LANEF No. ANR-10-LABX-51-01”. C.E. is supported by the MSCA Cofund QuanG (Grant Number: 101081458), funded by the European Union. The authors acknowledge the assistance of the staff of the Grenoble Advanced Technological Platform (PTA).

Supporting Information Available

See the Supporting Information for additional details about simulation of ion implantation, optical properties of single W centers in unpatterned SOI, finite-difference time-domain simulations, single W centers hunting strategy, and estimation of the zero-phonon emission rate for the CBG-coupled W center.

References

- (1) Silverstone, J. W.; Bonneau, D.; O'Brien, J. L.; Thompson, M. G. Silicon Quantum Photonics. *IEEE Journal of Selected Topics in Quantum Electronics* **2016**, *22*, 390–402.
- (2) Wang, J.; Sciarrino, F.; Laing, A.; Thompson, M. G. Integrated photonic quantum technologies. *Nature Photonics* **2020**, *14*, 273–284.
- (3) Singh, A.; Li, Q.; Liu, S.; Yu, Y.; Lu, X.; Schneider, C.; Höfling, S.; Lawall, J.; Verma, V.; Mirin, R.; Nam, S. W.; Liu, J.; Srinivasan, K. Quantum frequency conversion of a quantum dot single-photon source on a nanophotonic chip. *Optica* **2019**, *6*, 563–569.
- (4) Bauer, S.; Wang, D.; Hoppe, N.; Nawrath, C.; Fischer, J.; Witz, N.; Kaschel, M.; Schweikert, C.; Jetter, M.; Portalupi, S. L.; Berroth, M.; Michler, P. Achieving stable fiber coupling of quantum dot telecom C-band single-photons to an SOI photonic device. *Applied Physics Letters* **2021**, *119*, 211101.
- (5) Dibos, A. M.; Raha, M.; Phenicie, C. M.; Thompson, J. D. Atomic Source of Single Photons in the Telecom Band. *Physical Review Letters* **2018**, *120*, 243601.
- (6) Elshaari, A. W.; Pernice, W.; Srinivasan, K.; Benson, O.; Zwiller, V. Hybrid integrated quantum photonic circuits. *Nature Photonics* **2020**, *14*, 285–298.

- (7) Katsumi, R.; Ota, Y.; Tajiri, T.; Kakuda, M.; Iwamoto, S.; Akiyama, H.; Arakawa, Y. Unidirectional output from a quantum-dot single-photon source hybrid integrated on silicon. *Optics Express* **2021**, *29*, 37117–37127.
- (8) Redjem, W. et al. Single artificial atoms in silicon emitting at telecom wavelengths. *Nature Electronics* **2020**, *3*, 738–743.
- (9) Hollenbach, M.; Berencén, Y.; Kentsch, U.; Helm, M.; Astakhov, G. V. Engineering telecom single-photon emitters in silicon for scalable quantum photonics. *Optics Express* **2020**, *28*, 26111–26121.
- (10) Baron, Y.; Durand, A.; Herzig, T.; Khoury, M.; Pezzagna, S.; Meijer, J.; Robert-Philip, I.; Abbarchi, M.; Hartmann, J.-M.; Reboh, S.; Gérard, J.-M.; Jacques, V.; Cassabois, G.; Dréau, A. Single G centers in silicon fabricated by co-implantation with carbon and proton. *Applied Physics Letters* **2022**, *121*, 084003.
- (11) Hollenbach, M.; Klingner, N.; Jagtap, N. S.; Bischoff, L.; Fowley, C.; Kentsch, U.; Hlawacek, G.; Erbe, A.; Abrosimov, N. V.; Helm, M.; Berencén, Y.; Astakhov, G. V. Wafer-scale nanofabrication of telecom single-photon emitters in silicon. *Nature Communications* **2022**, *13*, 7683.
- (12) Zhiyenbayev, Y.; Redjem, W.; Ivanov, V.; Qarony, W.; Papapanos, C.; Simoni, J.; Liu, W.; Jhuria, K.; Tan, L. Z.; Schenkel, T.; Kanté, B. Scalable manufacturing of quantum light emitters in silicon under rapid thermal annealing. *Optics Express* **2023**, *31*, 8352–8362.
- (13) Andrini, G.; Zanelli, G.; Ditalia Tchernij, S.; Corte, E.; Nieto Hernández, E.; Verna, A.; Cocuzza, M.; Bernardi, E.; Virzì, S.; Traina, P.; Degiovanni, I. P.; Genovese, M.; Olivero, P.; Forneris, J. Activation of telecom emitters in silicon upon ion implantation and ns pulsed laser annealing. *Communications Materials* **2024**, *5*, 1–7.

- (14) Aberl, J.; Navarrete, E. P.; Karaman, M.; Enriquez, D. H.; Wilflingseder, C.; Salomon, A.; Primetzhofer, D.; Schubert, M. A.; Capellini, G.; Fromherz, T.; Deák, P.; Udvarhelyi, P.; Li, S.; Gali, A.; Brehm, M. All-Epitaxial Self-Assembly of Silicon Color Centers Confined Within Sub-Nanometer Thin Layers Using Ultra-Low Temperature Epitaxy. *Advanced Materials* **2024**, *n/a*, 2408424.
- (15) Durand, A.; Baron, Y.; Redjem, W.; Herzig, T.; Benali, A.; Pezzagna, S.; Meijer, J. H.; Kuznetsov, A. Y.; Gérard, J.-M.; Robert-Philip, I.; Abbarchi, M.; Jacques, V.; Cassabois, G.; Dréau, A. Broad Diversity of Near-Infrared Single-Photon Emitters in Silicon. *Physical Review Letters* **2021**, *126*, 083602.
- (16) Baron, Y. et al. Detection of Single W-Centers in Silicon. *ACS Photonics* **2022**, *9*, 2337–2345.
- (17) Higginbottom, D. B. et al. Optical observation of single spins in silicon. *Nature* **2022**, *607*, 266–270.
- (18) Prabhu, M.; Errando-Herranz, C.; De Santis, L.; Christen, I.; Chen, C.; Gerlach, C.; Englund, D. Individually addressable and spectrally programmable artificial atoms in silicon photonics. *Nature Communications* **2023**, *14*, 2380.
- (19) Durand, A. et al. Hopping of the Center-of-Mass of Single G Centers in Silicon-on-Insulator. *Phys. Rev. X* **2024**, *14*, 041071.
- (20) Moreau, E.; Robert, I.; Gérard, J. M.; Abram, I.; Manin, L.; Thierry-Mieg, V. Single-mode solid-state single photon source based on isolated quantum dots in pillar microcavities. *Applied Physics Letters* **2001**, *79*, 2865–2867.
- (21) Islam, F.; Lee, C.-M.; Harper, S.; Rahaman, M. H.; Zhao, Y.; Vij, N. K.; Waks, E. Cavity-Enhanced Emission from a Silicon T Center. *Nano Letters* **2024**, *24*, 319–325.

- (22) Johnston, A.; Felix-Rendon, U.; Wong, Y.-E.; Chen, S. Cavity-coupled telecom atomic source in silicon. *Nature Communications* **2024**, *15*, 2350.
- (23) Saggio, V.; Errando-Herranz, C.; Gyger, S.; Panuski, C.; Prabhu, M.; De Santis, L.; Christen, I.; Ornelas-Huerta, D.; Raniwala, H.; Gerlach, C.; Colangelo, M.; Englund, D. Cavity-enhanced single artificial atoms in silicon. *Nature Communications* **2024**, *15*, 5296.
- (24) Redjem, W.; Zhiyenbayev, Y.; Qarony, W.; Ivanov, V.; Papapanos, C.; Liu, W.; Jhuria, K.; Al Balushi, Z. Y.; Dhuey, S.; Schwartzberg, A.; Tan, L. Z.; Schenkel, T.; Kanté, B. All-silicon quantum light source by embedding an atomic emissive center in a nanophotonic cavity. *Nature Communications* **2023**, *14*, 3321.
- (25) Gritsch, A.; Ulanowski, A.; Reiserer, A. Purcell enhancement of single-photon emitters in silicon. *Optica* **2023**, *10*, 783–789.
- (26) Lefaucher, B. et al. Cavity-enhanced zero-phonon emission from an ensemble of G centers in a silicon-on-insulator microring. *Applied Physics Letters* **2023**, *122*, 061109.
- (27) Durand, A.; Baron, Y.; Cache, F.; Herzig, T.; Khoury, M.; Pezzagna, S.; Meijer, J.; Hartmann, J.-M.; Reboh, S.; Abbarchi, M.; Robert-Philip, I.; Gérard, J.-M.; Jacques, V.; Cassabois, G.; Dréau, A. Genuine and faux single G centers in carbon-implanted silicon. *Physical Review B* **2024**, *110*, L020102.
- (28) Lefaucher, B.; Jager, J.-B.; Calvo, V.; Cache, F.; Durand, A.; Jacques, V.; Robert-Philip, I.; Cassabois, G.; Baron, Y.; Mazen, F.; Kerdilès, S.; Reboh, S.; Dréau, A.; Gérard, J.-M. Purcell Enhancement of Silicon W Centers in Circular Bragg Grating Cavities. *ACS Photonics* **2024**, *11*, 24–32.
- (29) Veetil, V. K.; Song, J.; Namboodiri, P. N.; Ebadollahi, N.; Chanana, A.; Katzenmeyer, A. M.; Pederson, C.; Pomeroy, J. M.; Chiles, J.; Shainline, J.; Srinivasan, K.;

- Davanco, M.; Pelton, M. Enhanced zero-phonon line emission from an ensemble of W centers in circular and bowtie Bragg grating cavities. *Nanophotonics* **2024**, *n/a*.
- (30) Li, L.; Chen, E. H.; Zheng, J.; Mouradian, S. L.; Dolde, F.; Schröder, T.; Karaveli, S.; Markham, M. L.; Twitchen, D. J.; Englund, D. Efficient Photon Collection from a Nitrogen Vacancy Center in a Circular Bullseye Grating. *Nano Letters* **2015**, *15*, 1493–1497.
- (31) Davanço, M.; Rakher, M. T.; Schuh, D.; Badolato, A.; Srinivasan, K. A circular dielectric grating for vertical extraction of single quantum dot emission. *Applied Physics Letters* **2011**, *99*, 041102.
- (32) Wang, H. et al. On-Demand Semiconductor Source of Entangled Photons Which Simultaneously Has High Fidelity, Efficiency, and Indistinguishability. *Physical Review Letters* **2019**, *122*, 113602.
- (33) Kolatschek, S.; Nawrath, C.; Bauer, S.; Huang, J.; Fischer, J.; Sittig, R.; Jetter, M.; Portalupi, S. L.; Michler, P. Bright Purcell Enhanced Single-Photon Source in the Telecom O-Band Based on a Quantum Dot in a Circular Bragg Grating. *Nano Letters* **2021**, *21*, 7740–7745.
- (34) Iff, O.; Buchinger, Q.; Moczala-Dusanowska, M.; Kamp, M.; Betzold, S.; Davanco, M.; Srinivasan, K.; Tongay, S.; Antón-Solanas, C.; Höfling, S.; Schneider, C. Purcell-Enhanced Single Photon Source Based on a Deterministically Placed WSe₂ Monolayer Quantum Dot in a Circular Bragg Grating Cavity. *Nano Letters* **2021**, *21*, 4715–4720.
- (35) Fröch, J. E.; Spencer, L. P.; Kianinia, M.; Totonjian, D. D.; Nguyen, M.; Gottscholl, A.; Dyakonov, V.; Toth, M.; Kim, S.; Aharonovich, I. Coupling Spin Defects in Hexagonal Boron Nitride to Monolithic Bullseye Cavities. *Nano Letters* **2021**, *21*, 6549–6555.
- (36) Spinicelli, P.; Dréau, A.; Rondin, L.; Silva, F.; Achard, J.; Xavier, S.; Bansropun, S.; Debuisschert, T.; Pezzagna, S.; Meijer, J.; Jacques, V.; Roch, J.-F. Engineered arrays

- of nitrogen-vacancy color centers in diamond based on implantation of CN- molecules through nanoapertures. *New Journal of Physics* **2011**, *13*, 025014.
- (37) Sangtawesin, S.; Brundage, T. O.; Atkins, Z. J.; Petta, J. R. Highly tunable formation of nitrogen-vacancy centers via ion implantation. *Applied Physics Letters* **2014**, *105*, 063107.
- (38) Yang, Y.; Bao, J.; Wang, C.; Aziz, M. J. Sub-bandgap luminescence centers in silicon created by self-ion implantation and thermal annealing. *Journal of Applied Physics* **2010**, *107*, 123109.
- (39) Buckley, S. M.; Tait, A. N.; Moody, G.; Primavera, B.; Olson, S.; Herman, J.; Silverman, K. L.; Rao, S. P.; Nam, S. W.; Mirin, R. P.; Shainline, J. M. Optimization of photoluminescence from W centers in silicon-on-insulator. *Optics Express* **2020**, *28*, 16057–16072.
- (40) Sapienza, L.; Davanço, M.; Badolato, A.; Srinivasan, K. Nanoscale optical positioning of single quantum dots for bright and pure single-photon emission. *Nature Communications* **2015**, *6*, 7833.
- (41) Holewa, P. et al. High-throughput quantum photonic devices emitting indistinguishable photons in the telecom C-band. *Nature Communications* **2024**, *15*, 3358.
- (42) Rickert, L.; Kupko, T.; Rodt, S.; Reitzenstein, S.; Heindel, T. Optimized designs for telecom-wavelength quantum light sources based on hybrid circular Bragg gratings. *Optics Express* **2019**, *27*, 36824–36837.
- (43) Santori, C.; Pelton, M.; Solomon, G.; Dale, Y.; Yamamoto, Y. Triggered Single Photons from a Quantum Dot. *Physical Review Letters* **2001**, *86*, 1502–1505.
- (44) Santori, C.; Fattal, D.; Vuckovic, J.; Solomon, G. S.; Yamamoto, Y. Single-photon generation with InAs quantum dots. *New Journal of Physics* **2004**, *6*, 89.

- (45) Dalgarno, P. A.; McFarlane, J.; Brunner, D.; Lambert, R. W.; Gerardot, B. D.; Warburton, R. J.; Karrai, K.; Badolato, A.; Petroff, P. M. Hole recapture limited single photon generation from a single n-type charge-tunable quantum dot. *Applied Physics Letters* **2008**, *92*, 193103.
- (46) Velha, P.; Picard, E.; Charvolin, T.; Hadji, E.; Rodier, J. C.; Lalanne, P.; Peyrade, D. Ultra-High Q/V Fabry-Perot microcavity on SOI substrate. *Opt. Express* **2007**, *15*, 16090–16096.
- (47) Komza, L.; Samutpraphoot, P.; Odeh, M.; Tang, Y.-L.; Mathew, M.; Chang, J.; Song, H.; Kim, M.-K.; Xiong, Y.; Hautier, G.; Sipahigil, A. Indistinguishable photons from an artificial atom in silicon photonics. *Nature Communications* **2024**, *15*, 6920.
- (48) Day, A. M.; Sutula, M.; Dietz, J. R.; Raun, A.; Sukachev, D. D.; Bhaskar, M. K.; Hu, E. L. Electrical manipulation of telecom color centers in silicon. *Nature Communications* **2024**, *15*, 4722.
- (49) Ristori, A. et al. Strain Engineering of the Electronic States of Silicon-Based Quantum Emitters. *Advanced Optical Materials* **2024**, *12*, 2301608.

Supporting Information:

Bright single-photon source in a silicon chip by nanoscale positioning of a color center in a microcavity

Baptiste Lefaucher,^{†,§} Yoann Baron,^{‡,§} Jean-Baptiste Jager,[†] Vincent Calvo,[†]
Christian Elsässer,[†] Giuliano Coppola,[†] Frédéric Mazen,[‡] Sébastien Kerdilès,[‡] Félix
Cache,[¶] Anaïs Dréau,[¶] and Jean-Michel Gérard^{*,†}

[†]*Univ. Grenoble Alpes, CEA, Grenoble INP, IRIG, PHELIQS, 38000 Grenoble, France*

[‡]*Univ. Grenoble Alpes, CEA-LETI, Grenoble 38000, France*

[¶]*Laboratoire Charles Coulomb, Université de Montpellier and CNRS, Montpellier, France*

[§]*Contributed equally to this work*

E-mail: jean-michel.gerard@cea.fr

Contents

1	Optical measurement setup	S-3
2	Simulation of the Si⁺ ion implantation	S-4
2.1	Distribution of ions in the silicon-on-insulator layer	S-4
2.2	Distribution of ions in the PMMA layer	S-6
3	Single W centers in unpatterned silicon-on-insulator	S-7
3.1	Diameter of the nanoholes	S-7
3.2	Photoluminescence map before fabrication of the cavities	S-7
3.3	Optical properties of a single W center	S-8
4	Finite-Difference Time-Domain simulations	S-9
4.1	Optimization of the circular Bragg grating cavities	S-9
4.2	Effect of spectral detuning	S-11
5	Hunting for CBG cavities containing a single W center	S-12
6	Estimation of the zero-phonon emission rate	S-14
7	Scanning electron microscopy image of the cavity	S-17
	References	S-18

1 Optical measurement setup

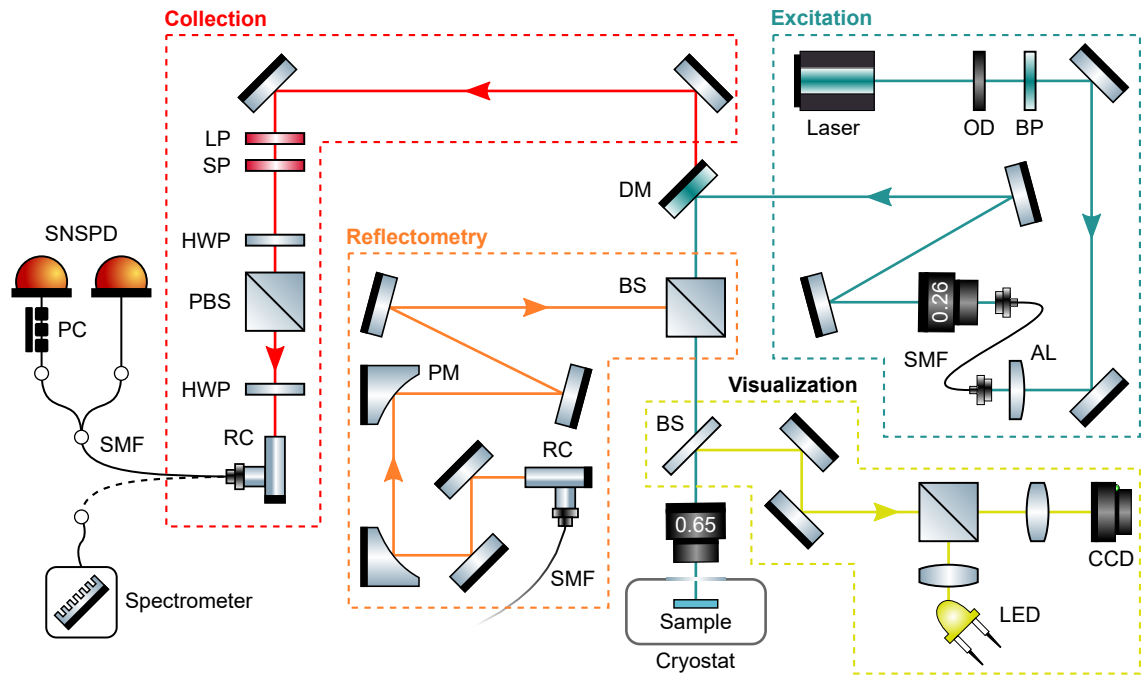


Figure S1: **Sketch of the optical measurement setup.** AL: aspheric lens. BP: band-pass filter. BS: beamsplitter. DM: dichroic mirror. HWP: half waveplate. LP: longpass filter. OD: optical density. PBS: polarizing beamsplitter. PC: polarization controller. PM: parabolic mirror. RC: reflective collimator. SMF: single mode fiber. SNSPD: superconducting nanowire single photon detector. SP: shortpass filter.

2 Simulation of the Si⁺ ion implantation

2.1 Distribution of ions in the silicon-on-insulator layer

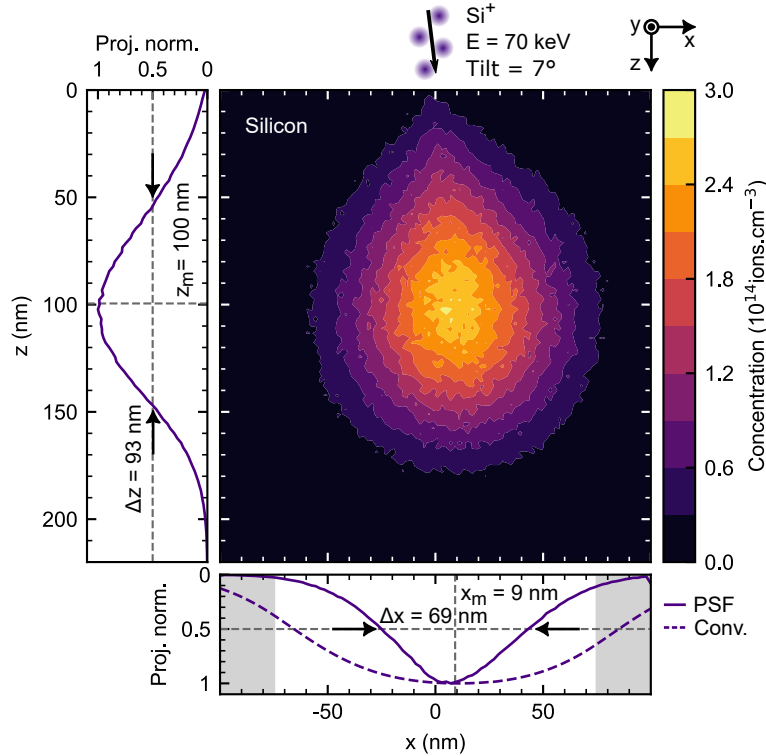


Figure S2: **Spatial distribution of Si⁺ ions implanted in the silicon-on-insulator layer.** The ions are implanted with an energy of 70 keV, 7° tilt, and a dose of 10^{11} cm^{-2} . The data are obtained from a 3D Monte Carlo simulation with 10^6 repetitions using the SRIM software. The left panel displays the projection of the distribution on the z axis. In the bottom panel, the full line indicates the point spread function (PSF) of the implanted ions, i.e. the projection of the distribution on the x axis for a single impact point. The dashed line corresponds to the convolution of the PSF with a disk of 150 nm diameter, delimited by the grey shaded area, corresponding to the nanohole diameter in the PMMA mask.

A 3D Monte Carlo simulation of the Si⁺ implantation of the silicon-on-insulator (SOI) wafer is performed using the Stopping and Range of Ions in Matter software (SRIM).^{S1} The result of the simulation is presented in Figure S2. The point of coordinates $(x, y, z)=(0,0,0)$, indicated by the arrow on top, is the impact point of the ions on the top surface of the silicon layer. The ions are implanted with an energy of 70 keV, with a tilt of 7° with respect to the

z axis in the xz plane. The simulation is performed with 10^6 repetitions.

The 2D plot represents the concentration of ions projected onto the xz plane, for a dose of 10^{11} ions.cm⁻². The projection of the distribution on the z axis is displayed in the left panel, showing that the ions are implanted at an average depth $z_m = 100$ nm with a FWHM of 93 nm. The projection on the x axis, in the bottom panel, shows that the ions are implanted at an average distance $x_m = 9$ nm from the impact point along the x axis, with a FWHM of 69 nm.

In previous work using similar implantation dose and annealing temperature, we have demonstrated that the distribution of W centers matches the vertical distribution of implanted Si⁺ ions relatively well.^{S2} The lateral spread of the W centers can therefore be tentatively estimated as the convolution between the lateral point spread function of the Si⁺ ions (plotted in full line in the bottom panel) and a disk of 150 nm diameter, corresponding to the nanohole diameter in the PMMA mask. The resulting distribution is plotted in dashed line. Considering that the cavities are positioned with an accuracy better than 30 nm, the W centers have near-unity probability to be located less than 120 nm away from the center of the cavity, and therefore couple to the main antinode of the electric field (see Figure 1(e) in the main text). This point is confirmed by the observation of numerous bright W centers in the sample (see Figure S8).

2.2 Distribution of ions in the PMMA layer

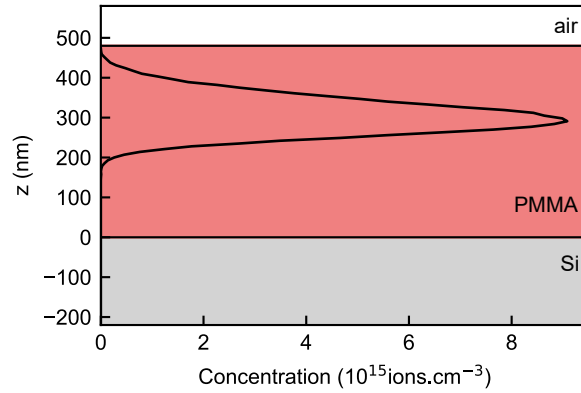


Figure S3: **Distribution of Si⁺ ions implanted in the PMMA layer**, obtained using the procedure described in the previous section. The PMMA layer has a thickness of 480 nm. The ions have an average position $z_m = 306$ nm, corresponding to a projecting range $R_p = 174$ nm from the air/PMMA interface.

3 Single W centers in unpatterned silicon-on-insulator

3.1 Diameter of the nanoholes

Table S1: Diameter of the nanoholes in the polymethyl methacrylate (PMMA) mask for Si⁺ implantation. Each set of nanoholes contains 12+ different diameter values. n is used as a label to identify the diameter of a nanohole as a function of its position in the set.

n	01	02	03	04	05	06	07	08	09	10	11	12
D (nm)	2000	1000	800	600	500	400	350	300	250	200	150	125

3.2 Photoluminescence map before fabrication of the cavities

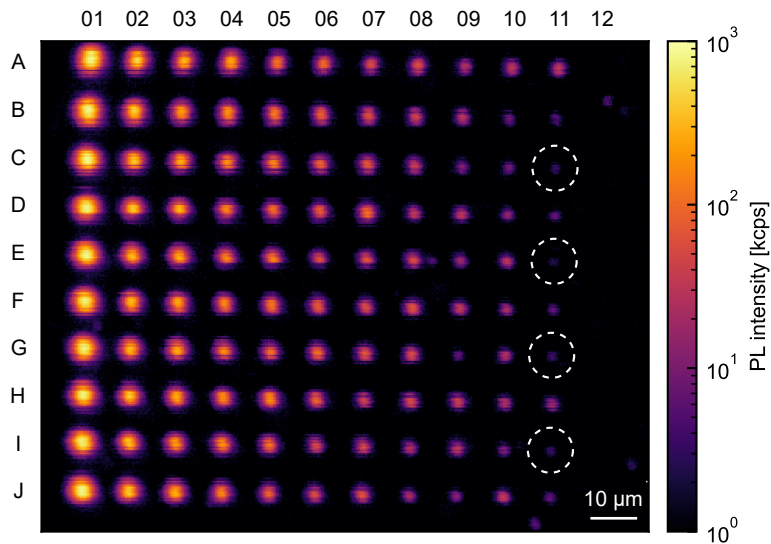


Figure S4: **PL map of the unpatterned silicon-on-insulator wafer**, at 10 K, under continuous-wave excitation with a power of 135 μ W. The integer labels on top of the map refer to the diameter of the nanoholes for each column (see Table S1). The letters on the left side are used as labels for the lines, all corresponding to the same set of nanoholes. The dashed circles in the 11th column ($D = 150$ nm) indicate PL spots that have been identified as single W centers. These spots have an average background-corrected intensity of 3.2 ± 0.8 kcps.

3.3 Optical properties of a single W center

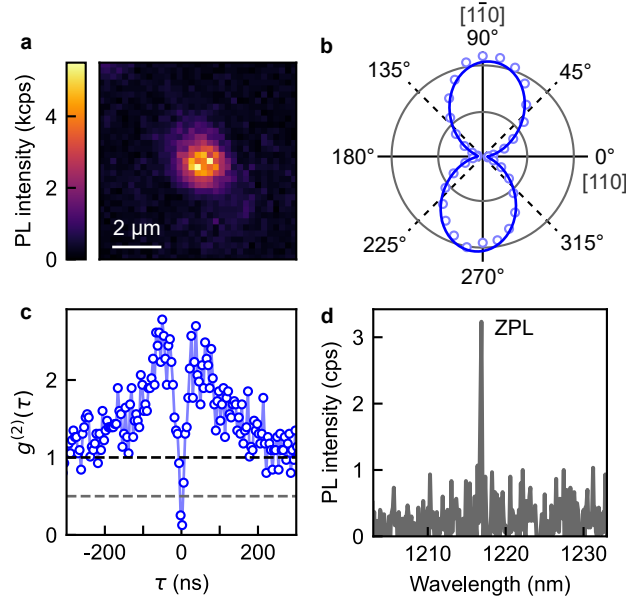


Figure S5: **Optical properties of a single W center in unpatterned silicon-on-insulator.** **a**, PL map. **b**, Polarization diagram of the PL. Here, the PL is polarized along the $[1\bar{1}0]$ axis. For all studied W centers, the polarization is oriented along $[110]$ and $[1\bar{1}0]$, in agreement with previous work.^{S3} **c**, Second-order correlation histogram with 4 ns time bins. **d**, PL spectrum. The sharp peak at 1217 nm is unambiguously identified as the zero-phonon line (ZPL) of a single W center. The map, polarization diagram and spectrum are obtained under continuous-wave excitation with a power of 135 μW . The second-order correlation histogram is obtained with a power of 13 μW . All measurements are performed at 10 K.

4 Finite-Difference Time-Domain simulations

4.1 Optimization of the circular Bragg grating cavities

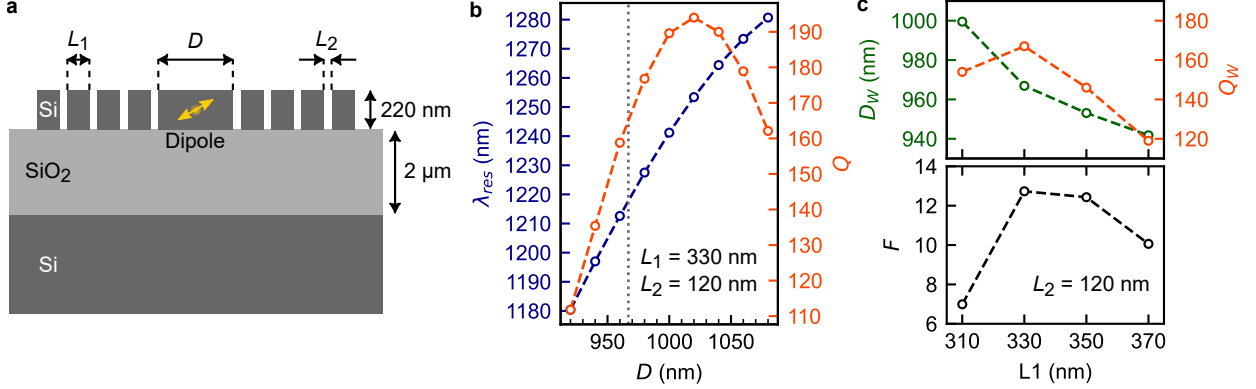


Figure S6: **Optimization of the CBG cavities.** **a**, Schematic of the design with the relevant dimensions and parameters. **b**, Wavelength λ_{res} and quality factor Q of the resonant mode as a function of the diameter D of the central disk, for $L_1 = 330$ nm and $L_2 = 120$ nm. **c**, Diameter D_W allowing resonance at 1218 nm as a function of L_1 , and corresponding quality factor Q_W . For each set of parameters, the Purcell factor F is calculated for a W center located at the center of the cavity.

Finite-Difference Time-Domain (FDTD) simulations are performed using the FULL-WAVE solver from Synopsys in order to optimize the Circular Bragg Grating (CBG) cavity design. The simulations consist in calculation of transient and steady-state electromagnetic fields by resolving time-dependent Maxwell equations in a discretized volume of space. A sectional view of the 3D simulation box is represented in Figure S6(a). The top silicon layer has a fixed thickness of 220 nm, and the CBG cavity has a free diameter D , rings width L_1 and gap-width L_2 . The buried oxide layer has a thickness of 2 μm . A dipole emitting at 1218 nm, oriented along the $\langle 111 \rangle$ direction, is placed at the core of the cavity.

The wavelength λ_{res} and quality factor Q of the resonant mode are determined using a cavity ringdown calculation. At time $t = 0$, the dipole flashes a pulse of light. A monitor placed in the vicinity of the dipole records the amplitude of the electric field as a function of time, until the field has almost entirely escaped from the cavity. The spectral lineshape $|E(\omega)|^2$ of the resonant mode is obtained by a fast Fourier transform of the time-trace. The

λ_{res} and Q values are obtained by fitting the lineshape to a Lorentzian function:

$$|E(\omega)|^2 \propto \frac{1}{1 + 4Q^2\left(\frac{\omega}{\omega_{res}} - 1\right)^2} \quad (\text{S.1})$$

where $\omega_{res} = 2\pi c/\lambda_{res}$ is the resonant frequency.

Figure S6(b) shows the wavelength and quality factor of the resonant mode as a function of D , for $L_1 = 330$ nm and $L_2 = 120$ nm. The grey dashed line indicates the diameter D_W for which $\lambda_{res} = 1218$ nm. The same series of calculations was performed for several L_1 and L_2 values. Figure S6(c) displays D_W as a function of L_1 , together with the associated quality factor Q_W . A maximum quality factor of 167 is obtained for $D_W = 967$ nm, $L_1 = 330$ nm and $L_2 = 120$ nm.

The Purcell factor F , defined as the ratio between the emission rate of the dipole in the cavity and in bulk silicon, is obtained by a calculation of the steady-state electric field in the cavity. At time $t = 0$, the dipole starts to emit continuous quasi-monochromatic radiation at 1218 nm, using a slow intensity ramp to avoid step-induced harmonics. The total emitted power is recorded by a monitor tightly localized around the dipole. The emitted power increases as the back-reflected electric field stimulates the emission of the dipole, until a stationary regime is reached. The Purcell factor is given by the normalized power value in the stationary regime. Figure S6(c) shows the Purcell factor for each (D_W, L_1) set obtained from ringdown calculation. A Purcell factor of 13 is obtained for $D_W = 967$ nm, $L_1 = 330$ nm and $L_2 = 120$ nm.

4.2 Effect of spectral detuning

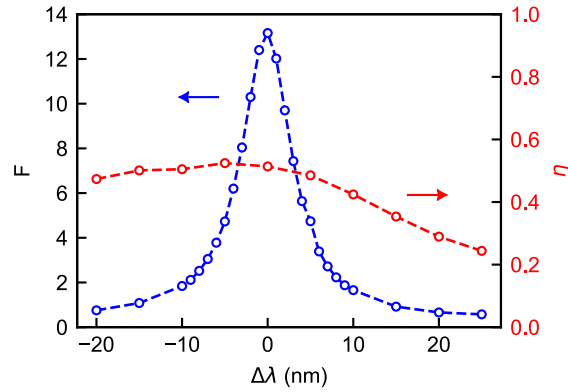


Figure S7: **Purcell factor and collection efficiency of the CBG cavity as a function of spectral detuning.** The spectral detuning $\Delta\lambda$ is the difference between the emission wavelength of the dipole and $\lambda_{res} = 1218$ nm. For estimating the collection efficiency, a monitor records the intensity radiated through a square aperture located in the farfield region above the dipole. The solid angle for this aperture is the same as for a microscope objective with a numerical aperture of 0.65. The collection efficiency η corresponds to the ratio between the intensity recorded by this monitor and the total intensity emitted by the dipole. A collection efficiency of 51% is obtained at zero-detuning, and remains above 40% in the $[-20 - +10]$ nm detuning range.

5 Hunting for CBG cavities containing a single W center

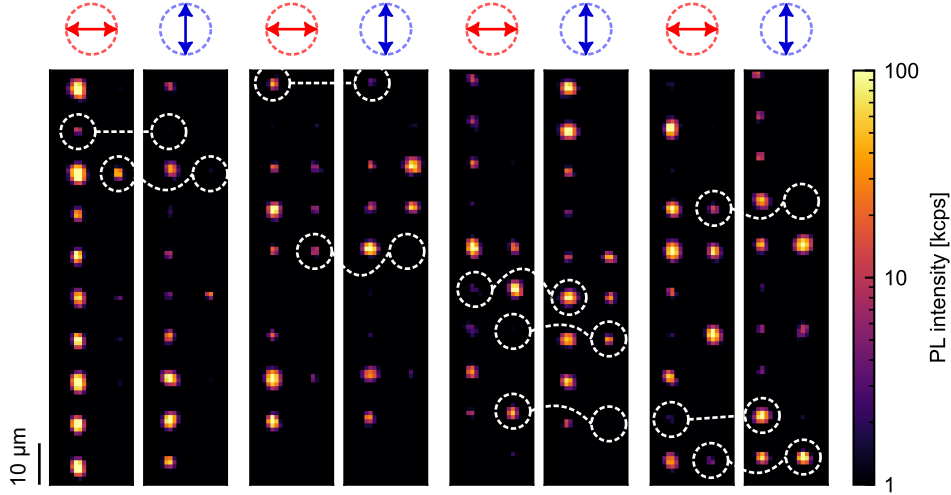


Figure S8: **Pairs of cross-polarized PL maps of CBG cavities**, under continuous-wave excitation with a power of $13 \mu\text{W}$. The pairs of circles indicate PL spots where a strong contrast is observed between horizontal and vertical polarization filtering conditions.

Due to the small mode volume of CBG cavities, the coupling strength between an emitter and the resonant mode is strongly sensitive to the location of the emitter. The intensity collected from an emitter is therefore dependent on its exact location, such that the intensity of a spot on a PL map is not proportionnal to the number of emitters. Consequently, single W centers cannot be solely identified from PL maps by simply investigating the PL count rates.

A hunting strategy based on the polarization of the PL has been devised. As the transition dipole of the W center is oriented along the $\langle 111 \rangle$ direction, the PL collected at normal incidence is either linearly polarized along $[110]$ or $[1\bar{1}0]$, depending on each emitter.^{S3} For the configuration of the experimental setup, these two orientations correspond to horizontally (H) and vertically (V) polarized light. As we use circular CBG cavities, we expect this property to be preserved also for single W in cavities. A single $[111]$ -oriented W center will therefore exhibit maximum and no signal when the detection polarization is set to H and V directions, respectively. H- and V-polarized PL spots are easily identified by performing pairs of PL maps with a polarization filter, where only H-polarized light is detected for the

first map and V-polarized light for the second map.

Figure S8 presents four pairs of such PL maps. The pairs of dashed white circles indicate spots for which a strong contrast of the PL signal is observed between the two orientations, indicating H- or V-polarized PL and therefore suggesting the presence of a single W center (or several emitters oriented along the same direction). Photon antibunching is systematically observed for all the investigated extinction spots. On the one hand, this demonstrates the efficiency of the hunting strategy to pre-identify single W centers. On the other hand, the results show that numerous bright sources are obtained using our nanofabrication method. For nanoholes with $D=150$ nm, we obtain single W centers for around 20 to 30 % of the spots. The statistical properties of the number of W centers per spot will be studied in more detail in the future.

For sake of completeness, we show in Figure S9 the polarisation diagram of the PL emission for the CBG cavity presented in the manuscript.

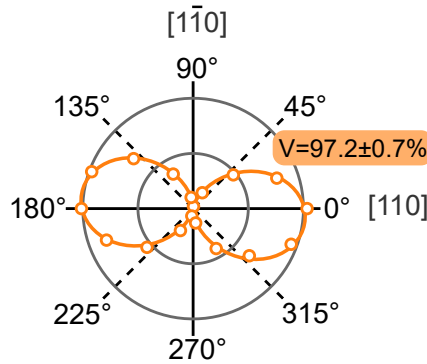


Figure S9: **Polarization diagram of the PL emission.** Here, the PL is polarized along the $[110]$ axis.

6 Estimation of the zero-phonon emission rate

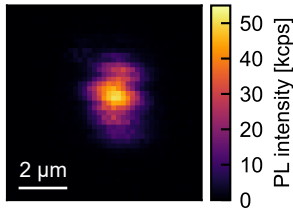


Figure S10: **PL map of the CBG-coupled W center under pulsed excitation.** The excitation laser has a repetition rate of 5 MHz and average power 17.5 μW . A maximum PL intensity around 52 kc/s is observed when the pump beam is located at the center of the cavity.

The W center under study exhibits a 7 ns lifetime of its excited state. Since we have no information of the magnitude of non-radiative processes, we use the PL intensity at saturation and a detailed analysis of the photon budget from generation to detection to estimate the emitter’s quantum efficiency and the zero-phonon emission rate. We define η_{ZPL} as the probability for the W center to relax through zero-phonon emission rather than other channels (non-radiative recombination, and phonon-assisted radiative recombination). We collect PL within the [1200, 1300] nm spectral window. Since the contribution of phonon-assisted processes to the PL is negligible, the PL intensity at saturation under pulsed excitation is proportional to η_{ZPL} and to the pump repetition rate:

$$\Gamma_d^{(pulsed)} = \eta_{ZPL} \times \eta_{coll} \times T_{fl} \times T_{setup} \times \eta_{SDE} \times \frac{\tau_{on}}{\tau_{on} + \tau_{off}} \times \Gamma_{exc} \quad (\text{S.2})$$

where:

- $\eta_{coll} = 51\%$ is the collection efficiency of the PL by the microscope objective with a numerical aperture of 0.65, estimated by FDTD simulation.
- $T_{fl} = 72\%$ is the transmission from the sample to the input of the *first lens*, which in our case is the microscope objective. The estimation is based on the transmission values provided by the manufacturers.

- $T_{setup} < 56\%$ is the transmission from the microscope objective to the photodetector, corresponding to the product of all the optics transmission values and fiber-coupling efficiencies. The estimation is an upper bound as it assumes perfect overlap between the PL mode and the fundamental mode of the collection fiber.
- $\eta_{SDE} = 81\%$ is the detection efficiency of the SNSPD, as provided by the manufacturer.
- $\tau_{on} = 153 \pm 4$ ns and $\tau_{off} = 741 \pm 6$ ns are the characteristic times of the photoblinking behaviour, which must be taken into account in order to estimate the quantum efficiency when the W center is in its optically active state.

As shown by Figure S10, the PL intensity at saturation for a pulsed pumping at 5 MHz is around 52 kcounts/s, so that we get from Equation S.2 $\eta_{ZPL} > 38\%$. Importantly, Equation S.2 is valid under the assumption that the average delay between successive detection events is much larger than the 29 ns recovery time of the SNSPD. This is the case as the repetition period is 200ns in our experiment. We have also implicitly assumed that one photon at most is detected for each pumping cycle, despite the fact that $A_0 \approx 0.51$ at saturation indicates that about two photons are emitted on average per pulse. This assumption is perfectly valid as the delay between the emission of the two photons (≈ 7 ns) is much shorter than the recovery time of the detector.

A lower bound of 38 % is estimated for the quantum efficiency when the emitter is in its optically active state. This value is certainly underestimated as it assumes that the best possible sample-to-detector transmission value is reached (perfect overlap between the PL mode and collection mode, aberration-free confocal microscope, no scattering by the optics, etc...). The zero-phonon emission rate for the W center under study, given by $\Gamma_{ZPL} = \eta_{ZPL}/\tau$ where $\tau = 7$ ns is the lifetime of the excited state, is therefore larger than $1/18$ ns⁻¹. This value should be compared with the zero-phonon emission of $1/134$ ns⁻¹ estimated for W centers in bulk silicon,^{S2} demonstrating Purcell enhancement of the zero-phonon emission rate for the cavity-coupled emitter by a factor $F > 7.2$. It is also worth

deriving an upper bound for η_{ZPL} . As the maximum Purcell enhancement of ZPL emission is 13 for W in CBG cavities, we get $\eta_{ZPL}^{max} = 13 / 134 \times \tau = 68 \%$.

Finally, it is also possible in principle to estimate the quantum efficiency η_{ZPL} from the PL intensity at saturation under continuous wave pumping:

$$I_{sat}^{(CW)} = \frac{\eta_{ZPL}}{\tau} \times \eta_{coll} \times T_{fl} \times T_{setup} \times \eta_{SDE} \times \frac{\tau_{on}}{\tau_{on} + \tau_{off}} \times \Gamma_{exc} \quad (\text{S.3})$$

From the 1.3×10^6 counts PL intensity at saturation, we get $\eta_{ZPL} > 33\%$, in agreement with the estimate obtained under pulsed pumping.

7 Scanning electron microscopy image of the cavity

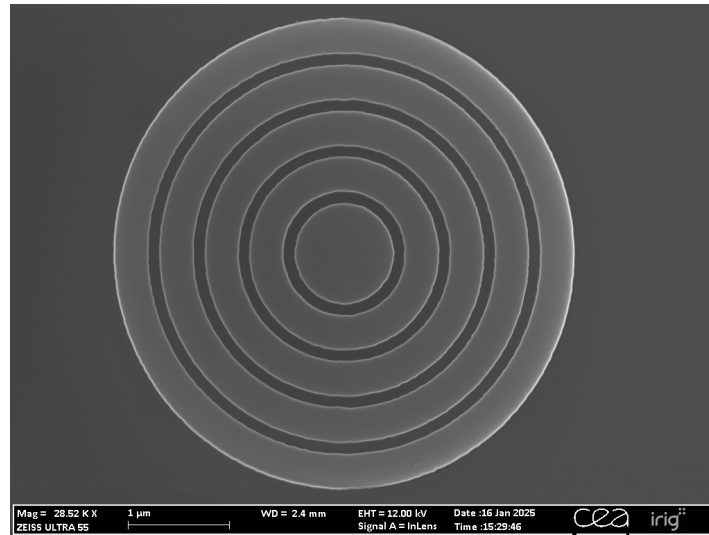


Figure S11: **Scanning electron microscopy image of a CBG cavity**, similar to the one containing the single W center studied in the manuscript.

References

(S1) See <http://www.srim.org/> for more information about the SRIM software.

(S2) Lefaucher, B.; Jager, J.-B.; Calvo, V.; Cache, F.; Durand, A.; Jacques, V.; Robert-Philip, I.; Cassabois, G.; Baron, Y.; Mazen, F.; Kerdilès, S.; Reboh, S.; Dréau, A.; Gérard, J.-M. Purcell Enhancement of Silicon W Centers in Circular Bragg Grating Cavities. *ACS Photonics* **2024**, *11* (1), 24-32.

(S3) Baron, Y.; Durand, A.; Udvarhelyi, P.; Herzig, T.; Khoury, M.; Pezzagna, S.; Meijer, J.; Robert-Philip, I.; Abbarchi, M.; Hartmann, J. M.; Mazzocchi, V.; Gérard, J.-M.; Gali, A.; Jacques, V.; Cassabois, G.; Dréau, A. Detection of Single W-Centers in Silicon. *ACS Photonics* **2022**, *9* (7), 2337-2345.